Draft version June 30, 2016
Preprint typeset using LaTeX style emulateapj v. 5/2/11

arXiv:1606.08847v1 [astro-ph.GA] 28 Jun 2016

THE DRAGONFLY NEARBY GALAXIES SURVEY. I. SUBSTANTIAL VARIATION IN THE DIFFUSE STELLAR HALOS AROUND SPIRAL GALAXIES

Allison Merritt[1], Pieter van Dokkum[1], Roberto Abraham[2,3] & Jielai Zhang[2,3]

Draft version June 30, 2016

ABSTRACT

Galaxies are thought to grow through accretion; as less massive galaxies are disrupted and merge over time, their debris results in diffuse, clumpy stellar halos enveloping the central galaxy. Here we present a study of the variation in the stellar halos of galaxies, using data from the Dragonfly Nearby Galaxies Survey (DNGS). The survey consists of wide field, deep ($\mu_g > 31$ mag arcsec^{-2}) optical imaging of nearby galaxies using the Dragonfly Telephoto Array. Our sample includes eight spiral galaxies with stellar masses similar to that of the Milky Way, inclinations of $16 - 90$ degrees and distances between $7 - 18$ Mpc. We construct stellar mass surface density profiles from the observed g-band surface brightness in combination with the $g-r$ color as a function of radius, and compute the halo fractions from the excess stellar mass (relative to a disk+bulge fit) beyond 5 half-mass radii. We find a mean halo fraction of 0.009 ± 0.005 and a large RMS scatter of $1.01^{+0.9}_{-0.26}$ dex. The peak-to-peak scatter is a factor of > 100 – while some galaxies feature strongly structured halos resembling that of M31, three of the eight have halos that are completely undetected in our data. We conclude that spiral galaxies as a class exhibit a rich variety in stellar halo properties, implying that their assembly histories have been highly non-uniform. We find no convincing evidence for an environmental or stellar mass dependence of the halo fraction in the sample.

Subject headings: galaxies: spirals — galaxies: halos — galaxies: stellar content — galaxies: structure

1. INTRODUCTION

In a ΛCDM universe, the hierarchical growth of dark matter structures is mirrored by the buildup of galaxies through a series of mergers and low mass accretion events (Purcell et al. 2007; Johnston et al. 2008; De Lucia & Helmi 2008; Cooper et al. 2013; Pillepich et al. 2014). Stars stripped from satellite galaxies during this process come to reside in diffuse and highly structured stellar halos enveloping the central galaxy, which, as a consequence of the relatively long dynamical timescales in the outskirts of galaxies, retain a "memory" of past accretion events. Understanding the accretion histories of individual galaxies, then, amounts to characterizing their stellar halos.

The recent non-detection of the stellar halo of the massive spiral galaxy M101 down to 32 mag arcsec^{-2} by van Dokkum et al. (2014) stands in contrast to the extensively studied stellar halos of the Milky Way (e.g., Majewski et al. 2003; Belokurov et al. 2006; McConnachie et al. 2006; Carollo et al. 2007; Bell et al. 2008) and M31 (e.g., Ibata et al. 2001; Ferguson et al. 2002; Ibata et al. 2007; Richardson et al. 2008; McConnachie et al. 2009; Gilbert et al. 2012), and strongly suggests that the variation between the stellar halos of massive spiral galaxies may be greater than previously thought.

Despite results from several studies which demonstrate that the scatter in the stellar populations (Seth et al. 2005; Mouhcine et al. 2007; Monachesi et al. 2013, 2015), amount of substructure (Bland-Hawthorn et al. 2005; Mouhcine et al. 2010; Martínez-Delgado et al. 2010; Miskolczi et al. 2011; Radburn-Smith et al. 2012; Okamoto et al. 2015), and even luminosity fractions (Shang et al. 1998; Barker et al. 2009; Tanaka et al. 2011; Vlajić et al. 2011; Barker et al. 2012; Bakos & Trujillo 2012) of stellar halos are qualitatively consistent with expectations from theory, the *stellar masses* of these halos, which in principle provide a robust point of comparison, in general remain unexplored (with only a few exceptions outside of the Local Group, e.g. Seth et al. 2007; Bailin et al. 2011; Greggio et al. 2014; van Dokkum et al. 2014; Streich et al. 2015).

The main difficulty in measuring stellar masses is the need to characterize both the global structure of the stellar halo and its constituent stellar populations. Star counts surveys, which are capable of constructing color and metallicity profiles for the stellar halos of nearby galaxies (e.g. Monachesi et al. 2015), are typically restricted by sparse area coverage at larger distances, and the resulting profiles are thus susceptible to the presence of underlying substructure and not guaranteed to reliably represent the halo on large scales. Integrated light surveys are more efficient, but these observations are commonly plagued by scattered light from bright stars or the dense centers of galaxies. Light thrown into the wings of the point spread function (PSF) can masquerade as a stellar halo (de Jong 2008; Sandin 2014), and must be carefully controlled for or removed (Slater et al. 2009; Duc et al. 2015). Accordingly, measurements of stellar halo masses must rely on assumptions about at least one of these two components. The few measurements of stellar halo masses that have been made are – thus far – also not straightforward to compare, due to inconsistent methodology between different studies.

A more comprehensive understanding of the scatter in stellar halo mass fractions can be achieved through

[1] Department of Astronomy, Yale University, New Haven, CT, USA
[2] Department of Astronomy and Astrophysics, University of Toronto, Toronto, ON, Canada
[3] Dunlap Institute, University of Toronto

consistent measurements of the stellar halos of a larger sample of spiral galaxies. In this paper we present early results from the Dragonfly Nearby Galaxies Survey (DNGS). This is an ongoing photometric survey of nearby galaxies carried out with the Dragonfly Telephoto Array, a robotic refracting telescope optimized to cleanly detect low surface brightness emission Abraham & van Dokkum (2014). With its large field of view ($\sim 2^\circ \times 3^\circ$), Dragonfly provides panoramic images of each targeted galaxy.

Using deep (> 30 mag arcsec^{-2}) surface brightness and $g-r$ color profiles, we measure the stellar mass surface density profiles for eight objectively selected spiral galaxies. We derive the stellar halo masses for our sample from the surface density profiles and show that, even within a narrow mass range, the stellar halo mass fractions of spiral galaxies can vary by several orders of magnitude.

2. DATA

2.1. *Sample selection and observations*

We used the Dragonfly Telephoto Array (Abraham & van Dokkum 2014) to observe a sample of eight spiral galaxies. The array was used in an 8-lens configuration, prior to its upgrade to the present 48-lens configuration. The sample covers six separate Dragonfly fields, corresponding to a total area of ~ 55 square degrees on the sky. The galaxies were selected on the basis of their absolute magnitude ($M_B < -19.3$), and lie at distances of $7-18$ Mpc.

These fields were observed as part of an ongoing photometric survey of nearby bright galaxies (DNGS). The selection criteria for DNGS are based on absolute magnitude and distance, such that we obtain volume-limited samples in different bins of absolute magnitude. Effectively, in each absolute magnitude bin, we select the nearest galaxies that are visible from the New Mexico Skies Observatory. The only additional criterion is that the galaxies have low Galactic cirrus in their immediate vicinity ($F_{100\mu\mathrm{m}} < 1.5$ mJy/Sr along the line of sight, from IRAS maps). We emphasize that we did not target galaxies on the basis of known tidal debris or any other physical property except absolute B band luminosity. For galaxy properties, see Table 1.

We observed our sample throughout 2013 and 2014. Typical per-night exposure times were 5400 s or 10,800 s, taken in 9-point dither patterns of 600s individual exposures. Offsets between dither positions were either $25'$ or $40'$. Typical total exposure times ranged from 15 to 20 hours per galaxy.

Considering the (very low) surface brightnesses of the features we intend to study, observing under optimal conditions is critical. To avoid the effects of scattered moonlight and significant atmospheric cirrus, we took care to observe only during clear, dark conditions. Frames with obvious cirrus-induced effects (manifesting as round "halos" surrounding bright stars) were removed from the final coadded images. Diffuse atmospheric cirrus is more difficult to avoid, in particular because it can drift unnoticed in and out of our field of view over the course of the night; however, we are able to identify its signature in our data by performing photometric calibrations on each individual frame (using SDSS stars as reference Abazajian et al. 2009) and excluding frames with discrepant photometric zeropoints on a given night. This procedure, which is remarkably effective, is described in detail in J. Zhang et al (in preparation).

2.2. *Background variations and PSF effects*

After dark subtraction and flat fielding, the data show residual gradients in the background of each individual frame, which are largely due to the changing sky background with zenith distance. We modeled these gradients in each individual frame with a second order polynomial, and subtracted them. All objects in the field were aggressively masked to prevent their flux from affecting the fit. Owing to the large dithers and the stability of the instrument, no further steps were necessary to flatten the images (further details can be found in van Dokkum et al. 2014).

Star subtraction was performed using a custom python pipeline that computes an empirical, spatially-varying composite PSF from Dragonfly images. First, we divided the image into $n \times n$ subframes (3×3 proved to be sufficient). An average unsaturated PSF was constructed in each subframe from a large number of unsaturated stars. To ensure that no galaxies or overly elongated stars were included in the PSF, we iteratively rejected individual candidate sources that deviated signficantly from the average PSF. Furthermore, flux from all neighboring objects was masked out during the average. For each star, the central region of the composite PSF was thus constructed from the unsaturated PSFs. To ensure smooth variation over the field, at any (x, y) position in the frame, the model PSF was a weighted average of the PSFs in the nearest subframes. The wings of the PSF were built from all saturated stars in the field (i.e., we did not account for spatial variations in the wings).

After background subtraction and star subtraction, the 1σ surface brightness limits of each final, coadded $g-$band frame are $29-29.8$ mag arcsec^{-2} in 60" $\times$ 60" boxes; or $28.6-29.2$ mag arcsec^{-2} in 12" regions (the size of a 6×6 binned pixel). To arrive at these values, we placed 100 boxes (of the aforementioned size) down in empty regions of our data and measured the variation in the average flux contained therein. In this study, however, we integrated the flux in 6×6 binned images over broad elliptical annuli, and as the sample galaxies span up to ~ 10 arcmin, we reach magnitudes of $31-32$ mag arcsec^{-2} in the surface brightness profiles. The actual limit is not the same in each field, as it depends on the number of foreground stars, the size of the galaxy, and the amount of foreground Galactic cirrus. The derivation of the errorbars in our profiles is discussed in Section 3.

3. RESULTS

The Dragonfly images of the eight spiral galaxies are shown in Figure 1. Each image is 30 arcmin on a side. The familiar high surface brightness regions of the galaxies are shown in color; the low surface brightness outskirts are shown in grey scale. The galaxies show a remarkable variation in their low surface brightness outskirts – NGC 1084 has a nearly spherical halo featuring a giant tidal tail, whereas both NGC 1042 and M101 show spiral arms down to very faint surface brightness levels. In the bottom right, we show what M31 looks

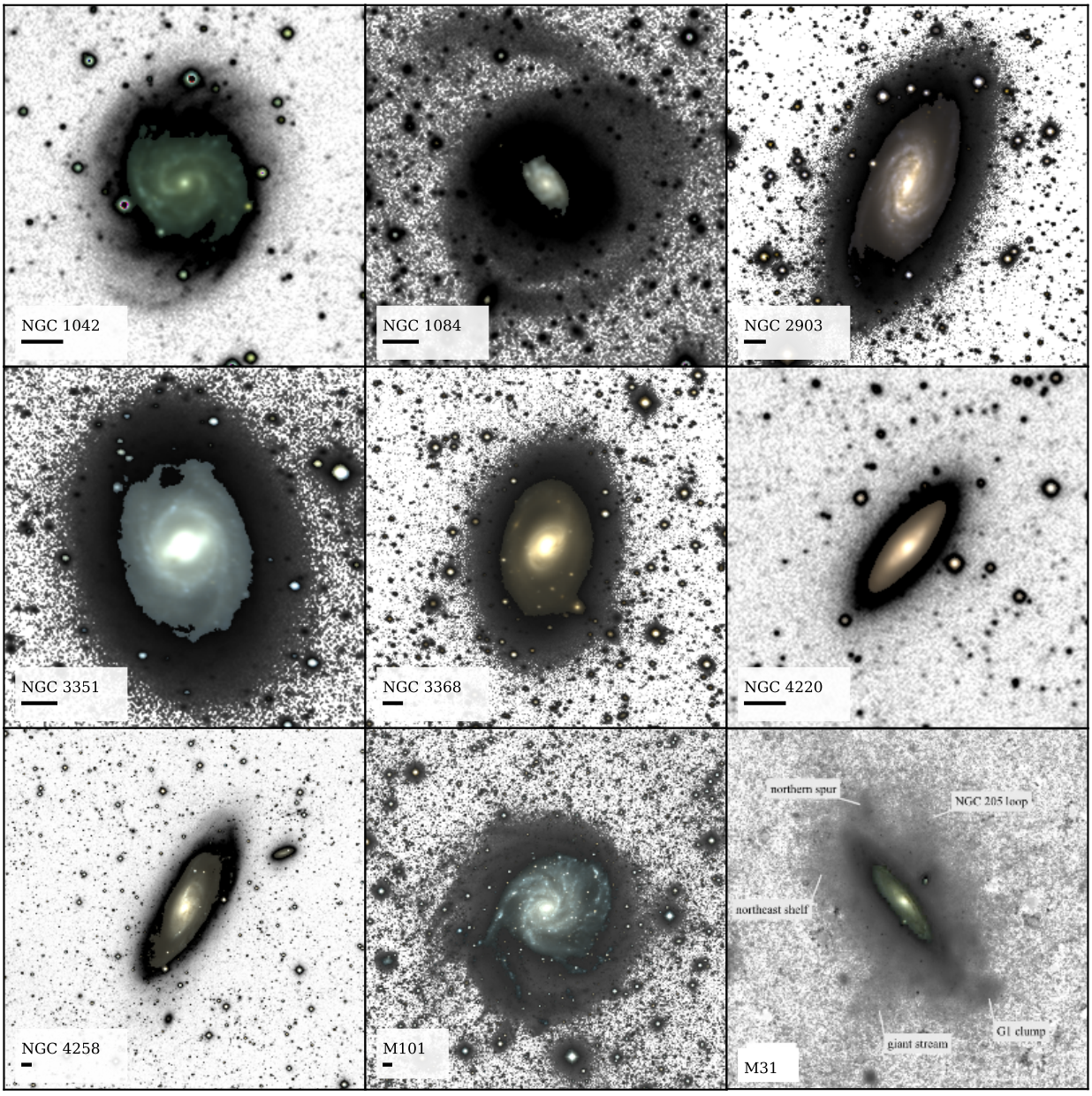

Figure 1. Images of each of the eight galaxies in this sample. The pseudo-color images were created from g and r band images for the high surface brightness regions, and the greyscale shows the lower surface brightness outskirts. The bottom right panel shows M31, created from a combination of Dragonfly and PAndAS data (McConnachie et al. 2009; Carlberg et al. 2011) and redshifted to a distance of 7 Mpc (van Dokkum et al. 2014). Black lines beneath each galaxy name indicate scales of 1 arcmin.

like when it is shifted out to a distance of 7 Mpc (comparable to M101) and placed in an empty region of a Dragonfly field (see van Dokkum et al. 2014). M31-like halos, characterized by significant substructure, are easily detectable in our data but appear to be atypical. In the following subsection, we quantify this observed variation in the stellar halos of Milky Way mass spiral galaxies using the surface brightness profiles of the galaxies.

3.1. *Surface brightness and stellar mass surface density profiles*

Both the surface brightness profiles and color profiles were derived from the binned (6×6) star-subtracted images. Elliptical isophotes were fit using the IRAF task `ellipse`, using logarithmic spacing of ellipses. First, we determined the positions of each isophote by running `ellipse` on the summed $g + r$ image. Next, we ran `ellipse` again on the individual images, holding those positions fixed. Any nearby galaxies or imperfectly sub-

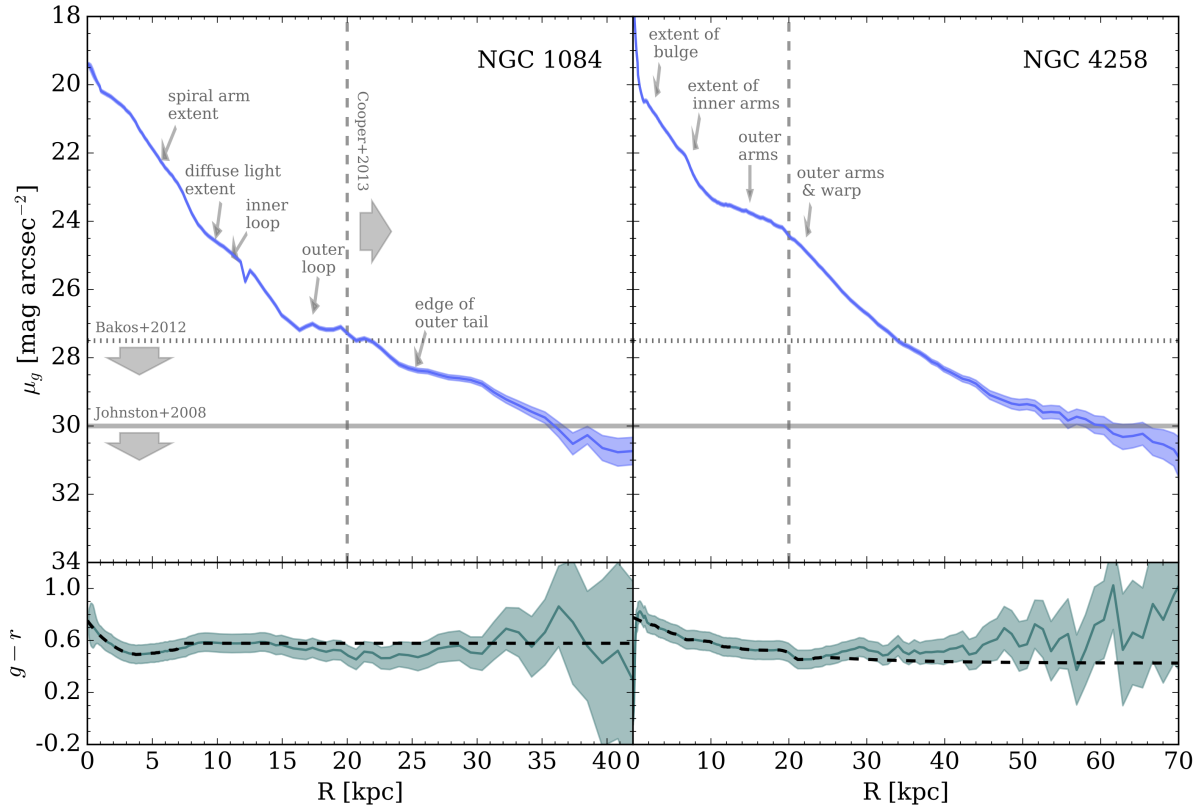

Figure 2. *Top panels*: Two example surface brightness profiles (and 1σ error bars) with labeled morphological features as a function of distance along the semi-major axis. Solid horizontal lines highlight the requisite depth to detect faint streams (Johnston et al. 2008), and dotted horizontal lines indicate the surface brightness limit below which M31-like halos are expected to dominate (Bakos & Trujillo 2012). The dashed vertical grey line shows the radius beyond which stellar halos are expected to dominate the light profile (Cooper et al. 2013). The features in the profile of NGC 1084 beyond ~ 7 kpc correspond to the stellar halo, whereas the profile of NGC 4258 is driven by the spiral disk out beyond ~ 20 kpc. *Bottom panels*: Observed and best fit $g-r$ color profiles. The shaded region around the observed color profiles represents the 1σ error.

tracted stars were masked during this procedure.

To determine the sky background, we measured the average flux in a circular annulus placed far from (but centered on) each galaxy. The exact distance was chosen to maximize the separation from the galaxy while avoiding any proximate galactic cirrus that might be present in the field (we selected targets to be in regions of low cirrus; however due to Dragonfly's large FOV this criterion does not exclude cirrus around the edges of the frame). To account for the error in the sky level (a dominant source of uncertainty for the outer isophotes), we measured the average flux in multiple circular annuli over a range of distances and calculated the peak-to-peak scatter between those values. The error bars on the surface brightness profiles therefore reflect this uncertainty as well as the error in the photometric zeropoint determination and the variation in counts along each particular isophote. Zeropoints were determined by calibrating to SDSS stars after correcting for galactic foreground extinction.

Example g-band surface brightness profiles for NGC 1084 and NGC 4258 are shown in Figure 2. The surface brightness profiles reach a signal-to-noise ratio of two at $30-32$ mag arcsec^{-2} in $g-$band (Table 2 indicates the radius where this occurs for each galaxy). The full set of surface brightness profiles are shown in Figure 3, and a comparison between our profiles and previously published work is shown in the Appendix. We note that one of the galaxies in our sample − M101 − has been investigated in previous work with Dragonfly (van Dokkum et al. 2014); we reanalyzed it here with the methods introduced in this paper for consistency.

We converted the surface brightness profiles to stellar mass surface density profiles (shown in Figure 4) using the relation between optical color and stellar mass-to-light ratios (Bell & de Jong 2001) and assuming a Chabrier IMF (Chabrier 2003). The error bars on the surface density profiles include the intrinsic scatter associated with this conversion (0.1 dex). The relation was determined from galaxies in the SDSS DR7 (Brinchmann et al. 2004) at low redshift ($0.045 < z < 0.055$) with similar stellar masses ($10 < \log_{10} M_{\rm stell} < 11$) and colors ($0.2 < g-r < 1.2$) as our sample, and takes the following form (van Dokkum et al. 2014):

$$\log\rho = -0.4(\mu_g - 29.23) + 1.49(g-r) + 4.58 \qquad (1)$$

To account for Dragonfly's low spatial resolution, we replaced the inner 2 kpc of each color profile with an

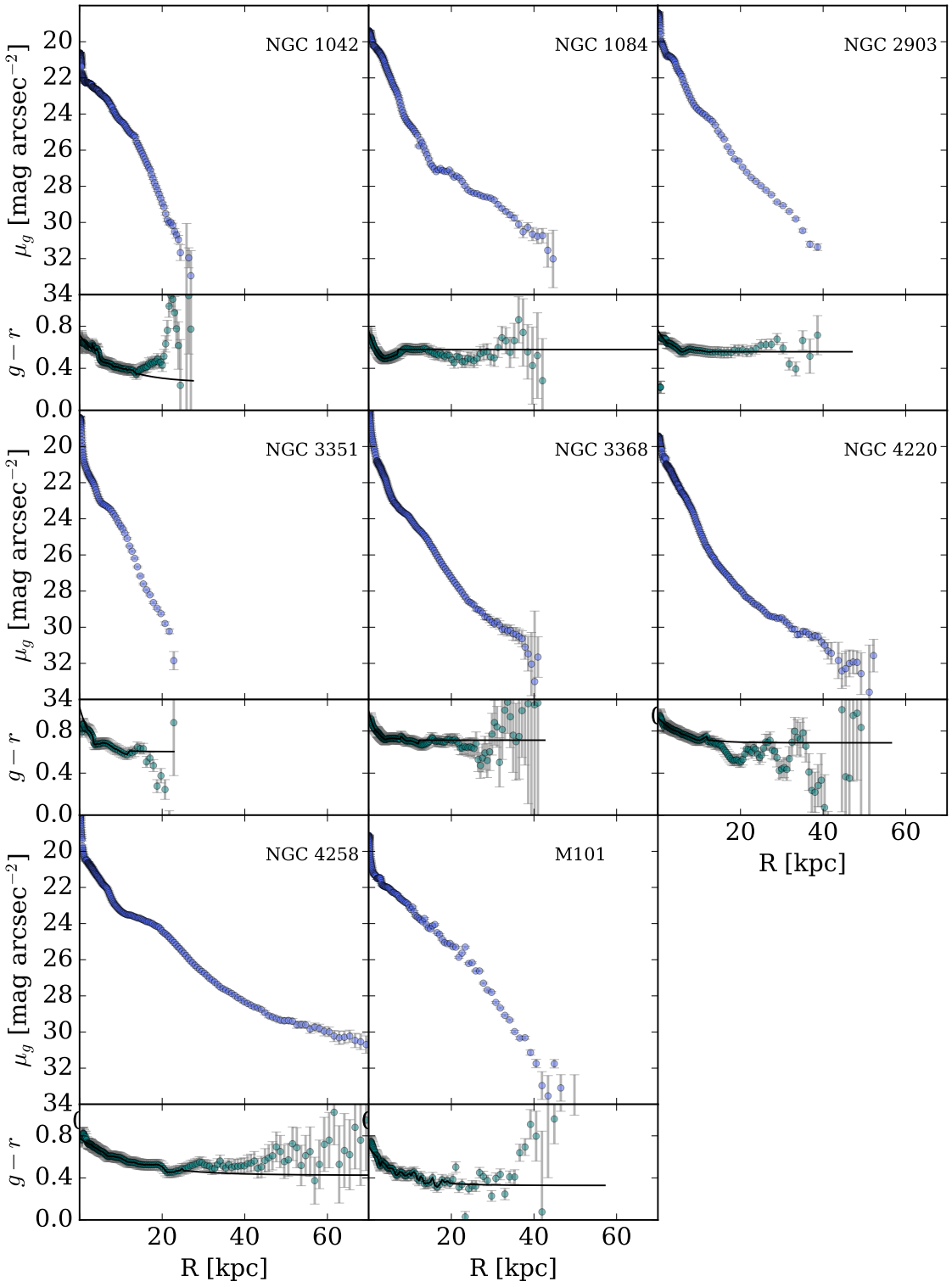

Figure 3. Same as Figure 2, but for the entire sample.

extrapolation of an exponential fit to the intermediate regions of the profile. We used the observed colors beyond 2 kpc, until the signal-to-noise becomes too low. The outermost regions of the color profile are a continuation of the same exponential fit, with the exception of NGC 1084, for which we assumed that the outer profile

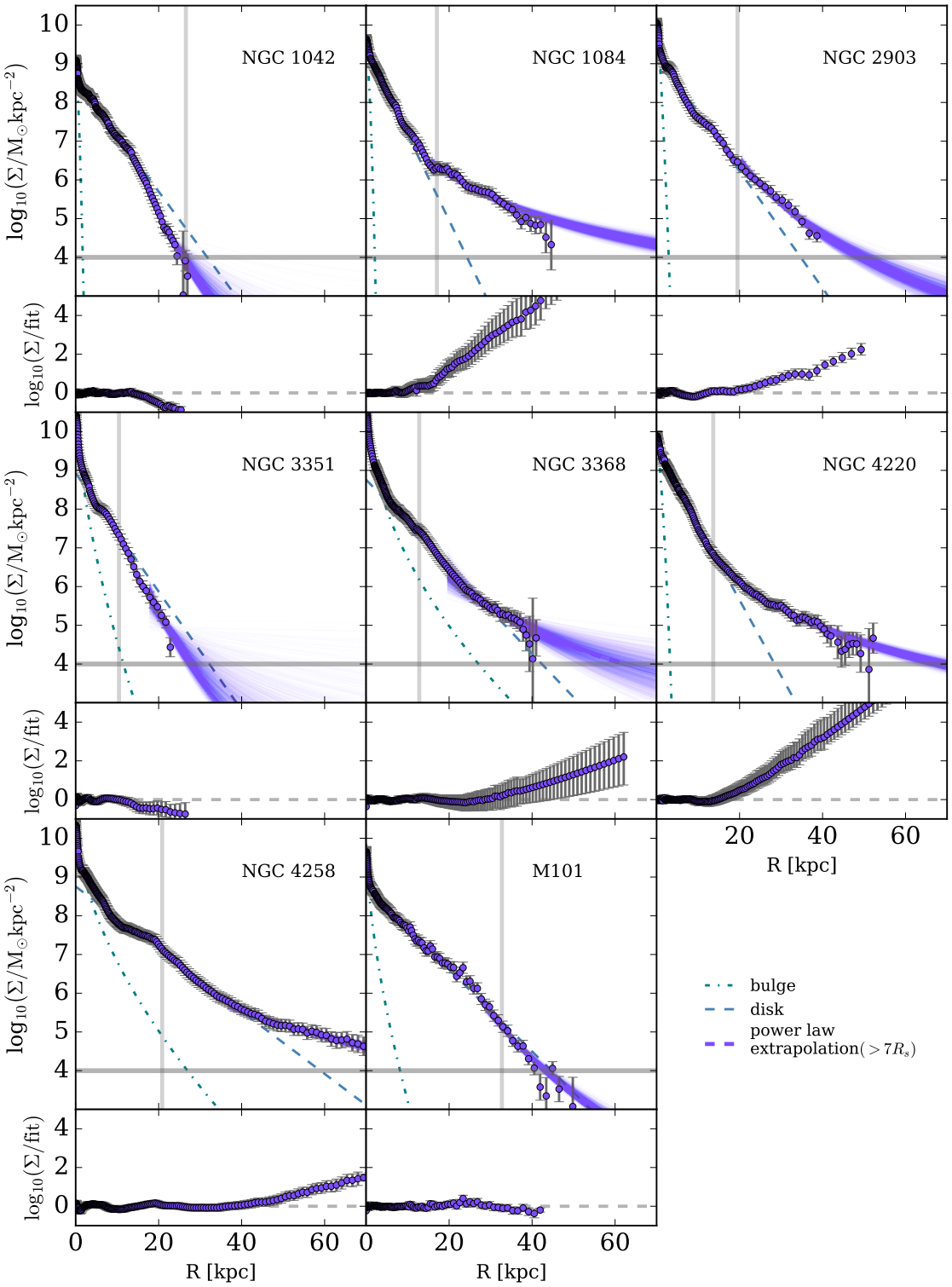

Figure 4. *Top panels*: Purple data points show the measured surface density profiles (and 1σ error bars). Dashed and faded solid purple lines indicate an extrapolation of this profile beyond $7R_s$ (vertical line) down to $10^4 M_\odot$ kpc $^{-2}$ (horizontal line). Best fit models of the disk and bulge are shown in green dot-dashed and blue dashed lines, respectively. See text for details. *Bottom panels*: Residuals after subtracting the bulge and disk models from the measured ($S/N > 2$) or extrapolated ($S/N < 2$) stellar mass surface density profile.

has the same color as the innermost smooth component of the halo (visible in the images).

3.2. *Stellar halos*

We define the stellar halo as the stellar mass ($M_{\rm stell}$) in excess of a disk+bulge model, measured outside of 5 half-mass radii (R_h) (thus, the stellar halo fraction $f_{\rm halo}(> 5R_h) = M_{\rm stell}(> 5R_h)/M_{\rm stell}$). If a stellar halo exists in a galaxy, it will only contribute significantly to the outermost regions of the galaxy (Abadi et al. 2006; Johnston et al. 2008; Font et al. 2011; Cooper et al. 2013; Pillepich et al. 2015), and we therefore expect that a disk+bulge model derived from the high surface brightness, inner regions (where we can visually verify that the dominant contributions to the light profile are the disk and bulge) will not be an adequate description for the lower surface brightness, outer regions.

We therefore determine stellar halo masses for each galaxy in the following way. First, we identified the farthest extent of spiral arms in the unbinned image (in order to utilize the higher spatial resolution; all subsequent measurements were done on binned images), and fit an exponential disk model to the stellar mass surface density profile over this region (Table 2). Next, we fit an additional bulge model, keeping the sersic index n as a free parameter. To ensure the robustness of our fits and to obtain reliable estimates of the uncertainties involved in this process, we used `emcee` (Foreman-Mackey et al. 2013), an implementation of the affine-invariant Monte Carlo Markov Chain (MCMC) ensemble sampler (Goodman & Weare 2010), to re-derive the maximum likelihood model. This time we fit all five parameters ($\Sigma_{0,\rm disk}$,R_s,$\Sigma_{0,\rm bulge}$,R_e,n) simultaneously. We adopted a two-stage method to initialize the `emcee` walkers. In a "burn-in" stage, we first initialized the walkers to small Gaussian distributions around our previous best-fit parameters and ran the MCMC sampler. We then identified the most likely solution from this run, and then ran the sampler again after re-initializing the walkers to (tighter) Gaussians around the new parameters. This allowed us to account for the possibility that our original best-fit model differs significantly from the most likely MCMC results, although we note that this step was unnecessary in most cases. To quantify the 1σ uncertainties for the final disk+bulge model, we sampled the posterior density functions (PDFs) ~ 2000 times and calculated the $16^{\rm th}$ and $84^{\rm th}$ percentiles from the resulting set of models as a function of radius.

In addition to the bulge+disk model, we also fit a power law model to the outskirts ($r > 7R_s$) of the stellar mass surface density profiles (Figure 4, applying the same methodology as before). These fits were used to extrapolate the stellar mass surface density profiles in our sample down to a uniform surface density of $10^4 M_\odot$ kpc^{-2}. The measured profiles were used where the S/N exceeds 2, and this fit was used when the S/N is lower than 2. We note that the amount of mass in the extrapolated region is always small compared to the total inferred halo mass; that is, the results are driven by the regions where the S/N exceeds 2 (except in the cases of NGC 1042 and NGC 1084; see below). The final disk and bulge fits are shown alongside the stellar mass surface density profiles for all galaxies in Figure 4. Table 2 contains the best-fit parameters for the disk, bulge, and power law fits.

With these models in hand, we calculated the excess stellar mass as the integral of the difference between the stellar mass surface density profile (measured or extrapolated) and the disk+bulge model outside of $5R_h$. The stellar halo mass fractions are shown in Figure 5 and quoted in Table 1.

The average stellar halo and its error bar were computed using the Kaplan-Meier product-limit estimator (Feigelson & Nelson 1985), a nonparametric maximum-likelihood estimator commonly used in "survival analysis" (that is, the set of statistical techniques for analyzing data that contains upper or lower limits). Using this method, we can obtain an estimate of the true distribution sampled by our data points as well as its mean and uncertainty.

To calculate the RMS scatter about the mean, we first calculate the difference between the mean as determined by the Kaplan-Meier estimator and the "direct" mean, that is, the mean that follows from treating the halo fractions of the three galaxies with no detected halo as measurements rather than upper limits. We then determined by what factor the three upper limits need to be lowered so that the direct mean equals the previously determined Kaplan-Meier estimator of the mean. The RMS is calculated by applying this factor to the three upper limits and then treating them in the same way as the other measurements. This procedure ensures that the mean and the RMS are obtained in a self-consistent way.

The average $f_{\rm halo}(> 5R_h)$ is 0.009 ± 0.005, and the RMS scatter is $1.01^{+0.09}_{-0.26}$ dex. For galaxies that are consistent with having no mass in the stellar halo (that is, $M_{\rm stell,halo} \sim 0$), we placed an upper limit on the halo fraction by assuming the existence of a halo with a constant surface density of $10^4 M_\odot$ kpc^{-2}. The excess stellar mass includes both smooth and structured halo components, and early results from Dragonfly demonstrated that the extensively studied halo of M31 would be readily detectable both in the data and by impact on the radial profile out to ~ 100 kpc (van Dokkum et al. 2014).

We use halo fractions computed from surface density profiles extrapolated down to $10^4 M_\odot$ kpc^{-2} in all cases except for NGC 1084 and NGC 1042. A single power law is not an appropriate model to fit to the outskirts of NGC 1084 since the surface density profile steepens beyond $7R_s$, and therefore the extrapolation is a clear overestimate (Figure 4). NGC 1042 is a non-detection, and its surface density profile reaches $10^4 M_\odot$ kpc^{-2} at approximately $5R_h$, causing the minimum extrapolated halo to be underestimated. We therefore consider the directly measured halo fractions to be more reliable for these two galaxies. If we were to use the extrapolated halo fractions for every galaxy, we would obtain an average value of $0.009^{+0.005}_{-0.006}$ with an RMS scatter of $1.03^{+0.08}_{-0.24}$ dex.

Two of the galaxies in our sample (NGC 3368 and NGC 4258) have larger error bars that are consistent with a halo fraction of zero (Figure 5). The large uncertainties are driven by the fact that the visible excess above the disk+bulge model (Figure 4) occurs at substantially larger radii than $5R_h$. If we were to measure the excess mass below a surface density threshold of $10^6 M_\odot$ kpc^{-2} (consistent with the profiles obtained by e.g., Cooper et al. 2013) instead of outside of $5R_h$, the halo fractions

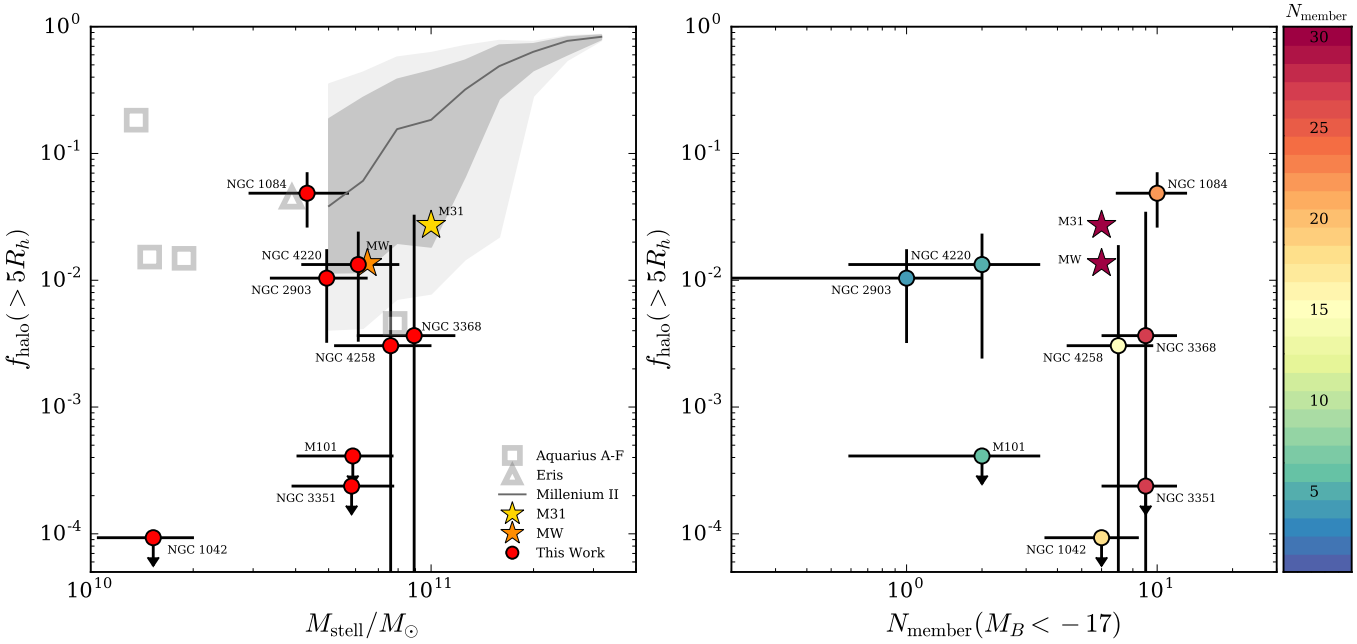

Figure 5. *Left*: The stellar halo mass fractions (and 1σ errors) for our sample, measured beyond $5R_h$ (red points). Values of $f_{\rm halo}$ for the Milky Way (Carollo et al. 2010) and M31 (Courteau et al. 2011) are shown for comparison (orange and gold stars, respectively), and have been scaled to the halo mass fraction outside of $5R_h$ assuming the structure of the halo of M31 (Irwin et al. 2005; Courteau et al. 2011). Predictions of $f_{\rm halo}$, measured over $3 \le r \le 280$ kpc from the Aquarius simulations (Cooper et al. 2010); over $r \ge 20$ kpc from the Eris simulation (Pillepich et al. 2015); and over $r \ge 3$ kpc from the Millenium II simulation (galaxies with B/T < 0.9 only; Cooper et al. 2013) are indicated by grey open squares, triangles, and shaded region, respectively. *Right*: Environmental richness is parametrized by the number of group members (Makarov & Karachentsev 2011) with $M_B < -17$. The color of each symbol corresponds to the *total* number of known group members for that particular galaxy. The stellar halo mass fractions do not appear to be a function of environment.

would become significant detections. Using this method we would derive an average halo fraction of 0.006 ± 0.003 with an RMS scatter of $0.95^{+0.08}_{-0.22}$ dex, which, encouragingly, is consistent with our original results. The decrease in the average halo arises mainly from NGC 1084, for which the deviation from disk+bulge occurs at surface densities higher than $10^6 M_\odot$ kpc^{-2}.

4. DISCUSSION

4.1. *A large variation in stellar halo mass fractions*

Confirming the visual impression of the galaxies in Figure 1, we find that the amount of mass in the stellar halo varies substantially between galaxies in the sample, despite their small range in stellar mass (Figure 5). The stellar halo fractions have a peak-to-peak span in $f_{\rm halo}(> 5R_h)$ of > 100, ranging from ≤ 0.0001 to 0.049 ± 0.02. The galaxy with the highest halo fraction is NGC 1084; this is also the only galaxy to feature a prominent tidal stream in its halo (consistent with previously published imaging; Martínez-Delgado et al. 2010). At the other extreme, three galaxies (NGC 1042, NGC 3351, and M101) are consistent with having *no* significant stellar halo, even at the detection limits of Dragonfly. We note that our results for NGC 3351 are qualitatively consistent with those of Watkins et al. (2014), who report a lack of evidence for recent accretion based on the exponential nature of the outer B-band surface brightness profile.

The galaxies cover only a small range in stellar mass, but we do not find a trend with mass within our sample (Figure 5, left panel). This is consistent with halo light fractions based on shallower observations of stacked individual galaxies with similar stellar masses in Stripe82 (Bakos & Trujillo 2012), although we measure a larger scatter and lower mean for our sample. Correlations between halo fraction and stellar mass are expected over broader ranges in mass (Pillepich et al. 2014), and there is observational evidence that stellar halos may become less common at lower stellar masses than those considered here (Vlajić et al. 2011; Bland-Hawthorn et al. 2005; Streich et al. 2015, but see also Belokurov & Koposov 2016). Moreover, the stellar halo fractions do not show any environmental dependence (right panel of Figure 5). Environment for each galaxy is parametrized by the number of bright ($M_B < -17$) associated group members, as reported in the MK group catalog (Makarov & Karachentsev 2011). Table 1 contains the number of group members for each galaxy. This lack of a trend between stellar halo fraction and environmental richness has also been seen in simulations (Lackner et al. 2012).

4.2. *Inclination effects*

Edge-on galaxies are generally considered ideal laboratories for stellar halo studies, as contamination from stars in the main disk and bulge is expected to fall off rapidly along the minor axis. As we did not select galaxies based on any intrinsic property other than luminosity, in our small sample we do not have any entirely edge-on galaxies. We extracted measuresments of inclination angles from the HyperLEDA database (Makarov et al. 2014).

The average inclination angle for galaxies in our full sample is 56.8°, and galaxies with and without detected

halos have average inclinations of 65.2 and 42.9, respectively. This is not necessarily surprising, since detecting faint halos is substantially more difficult to do in the presence of a relatively bright disk, and it is possible that the upper limits we derived for the three galaxies with non-detections are artificially lower as a consequence of this effect. However, we emphasize that the maximum likelihood disk+bulge model was determined in regions significantly interior to where the stellar halo mass was measured and we are therefore not relying on any ability to perform disk-halo decompositions at low surface density (and in fact, with the exception of M101, the galaxies for which no halo has been detected show a noticeable *deficit* of stellar mass surface density relative to the disk+bulge model). Furthermore, while on average the galaxies with detected halos are closer to being edge-on, the individual measurements range from 49.9° to $\sim 90°$, showing clear overlap with the sample with non-detections ($16.1° \leq i \leq 58°$) and demonstrating our ability to detect an excess of stellar mass even in only moderately inclined galaxies.

4.3. *Outer disk morphology*

Our method for measuring stellar halos relies on the assumption that the stellar mass surface density of the disk of the galaxy follows an exponential profile. This is a simplification, of course, as disks are known to frequently display more complex morphologies.

The surface brightness profiles of disk galaxies are only rarely a pure exponential (Type I) profile − approximately 60% of disks show a break in the radial profile at approximately $2.5R_{\rm disk}$, followed by a second, steeper exponential (Type II), and the remaining 30% (Type III) have a break followed by a shallower exponential (van der Kruit 1979; Pohlen & Trujillo 2006; Laine et al. 2014). Furthermore, Martín-Navarro et al. (2012) showed that truncations are also common in disks (at $3-5R_{\rm disk}$; van der Kruit & Searle 1982; Barteldrees & Dettmar 1994; Pohlen et al. 2000), although they occur at greater radial distances (lower surface brightness) and are thus more difficult to observe in face-on disks than in edge-on disks.

Stellar mass surface density profiles are less complicated. Bakos et al. (2008) demonstrated that both Type I and Type II disks have exponential stellar mass surface density profiles devoid of any significant break (a consequence of the characteristic "U" -shaped optical color profiles for Type II galaxies; see also Zheng et al. 2015; Ruiz-Lara et al. 2016). Truncations are still present, however, and the surface densities at which they occur are comparable to the surface densities at which stellar halos begin to dominate the total profile (Bakos & Trujillo 2012; Martín-Navarro et al. 2014).

Of the three galaxies in our sample that do not appear to have stellar halos, one has a stellar mass surface density that is a pure exponential (M101), and the others (NGC 1042 and NGC 3351) show truncations at $4.8R_{\rm disk}$ and $4.5R_{\rm disk}$, respectively. It is possible that each of these galaxies harbors a faint stellar halo that is either exactly balancing the drop in surface density due to a truncation (M101) or making the observed truncations shallower.

To investigate what the maximum halo contribution could be, we compute the stellar halo masses once more, assuming that the halos contain *all* the stellar mass beyond the last visible spiral arms. By definition, every galaxy in our sample now has a significant stellar halo, and the average halo fraction for the sample is 0.04±0.03. Importantly, the RMS scatter in halo fractions using this method is still very high, at $0.84^{+0.15}_{-0.36}$ dex. We are therefore confident that our primary finding of a substantial scatter between the stellar halos of massive spiral galaxies is robust to our assumptions of an exponential disk.

4.4. *Thick Disks?*

Further complications arise on the observational side, due to the possible contribution from thick disks, an additional, relatively low surface density component that ubiquitously exists in disk galaxies (Dalcanton & Bernstein 2002). It is possible, considering the disky isophotes of the low surface brightness regions of certain galaxies in our sample (Figure 1), that we have detected some thick disks and misinterpreted them as stellar halos. However, the mass in thick disks detected in external galaxies has been typically reported to be roughly 10% of the mass of the thin disk (Yoachim & Dalcanton 2006), and more recent estimates have increased this to be nearly comparable to the mass of the thin disk in some cases (Comerón et al. 2011), whereas the excess mass - to - disk mass ratios in our sample are are all $\lesssim 5\%$, with the majority $\lesssim 1\%$.

If the excess mass we measure *were* part of the thick disk, this would complicate inferences about the accretion histories of these galaxies. The formation mechansim of thick disks (or the stratified populations which mimic them, as suggested by Bovy et al. 2012) is still debated, but competing theories involve internal disk heating from interactions with spiral arms or star clusters (Loebman et al. 2011), formation as a thick disk at high redshift from material acquired during gas-rich mergers (Brook et al. 2004), buildup from shredded satellites accreted at low impact angle (Peñarrubia et al. 2006; Read et al. 2008), disk heating by massive accretion events (Abadi et al. 2003; Read et al. 2008), or, more likely, a combination of the above. Our data do not allow us to distinguish between these possibilities, but it is reasonable to assume that if we have observed thick disks, at least some of the stellar mass was accreted or indicative of a massive past accretion event.

More to the point, if part of the excess light is due to a thick disk component rather than a stellar halo, the mean halo mass fraction of the sample would be even lower. This in turn would strengthen our conclusion that M31 in particular has had an unusually active recent accretion history relative to other massive spiral galaxies.

4.5. *Stellar halo fractions in context*

Under the assumption that stellar halos are built primarily through the aggregation of individual accretion events over time, the large variation observed in halo mass fractions is reflective of the underlying variation in accretion histories of spiral galaxies. The accretion histories of the Milky Way and M31 are already suspected to have been significantly different, based on (among other metrics) the amount and global structure of light in their stellar halos (Carollo et al. 2010; Courteau et al. 2011; Deason et al. 2013). Similarly, from the halo fraction (and visible presence of a tidal stream) we can infer that

NGC 1084 has had a relatively active accretion history that continues to influence its growth.

It is possible that, given the low spatial resolution of Dragonfly (2.85 arcsec pixel^{-1}), the three galaxies that have no detected halos harbor faint, thin streams that are undetectable in our data, or that the stellar halos are diffuse enough to never surpass the surface density of the disk even at large radii. Still, our results place strong constraints on the possible nature of the accretion histories of these three galaxies. Specifically, we can rule out massive ($> 10^7 M_{\rm stell}$) accretion events over the past ~ 4.5 Gyr that would have resulted in a significant and irregularly structured halo, as well as a substantial and continuous infall of low mass systems, as this would produce a shallow power law profile similar to that of M31 (Deason et al. 2013).

The growth of stellar halos is known to be a stochastic process (Amorisco 2015), and simulations predict an RMS scatter in halo fractions of $0.5 - 0.6$ dex (e.g., Cooper et al. 2010, 2013, see Figure 5). The stellar halos of the eight spirals presented here have an RMS scatter of $1.01^{+0.09}_{-0.26}$ dex, approximately $2 - 3\times$ higher than theoretical expectations. Additionally, the average halo fraction for our sample is 0.009 ± 0.005, slightly lower than predicted values.

Such direct comparisons of average halo fractions between simulations and observations can be misleading, however, as the details of the simulation can have a substantial effect on the properties of the stellar halo. N-body simulations, for example, are significantly faster than hydrodynamic simulations and therefore have the advantage of being able to easily build up large samples of galaxies and stellar halos (a requirement for studying the intrinsic scatter in accretion histories); the trade-off is that any non-gravitational effects are neglected, and assigning stellar mass to DM particles is non-trivial and can lead to systematic changes in the concentration, morphology, extent, and amount of structure in stellar halos by factors of $2 - 7$ (Bailin et al. 2014).

Moreover, the stellar halo mass fraction and the accreted stellar mass fraction are not identical quantities. Two of the three simulations that we compare our results to in Figure 5 (Cooper et al. 2010, 2013) produce accretion-only stellar halos, but evidence (from observations and simulations alike) suggests that stars can come to reside in the stellar halo by means of in-situ star formation (Zolotov et al. 2009; Sheffield et al. 2012), stellar migration (Radburn-Smith et al. 2012), or ejection (Purcell et al. 2010; Dorman et al. 2013) (although beyond 20 kpc accreted stars are expected to contribute $\sim 97\%$ of the total stellar mass, according to Pillepich et al. 2015).

The majority of the mass in stellar halos is expected to be contributed by only a few relatively massive accretion events, which ultimately merge with the central galaxy and deposit most of their stars onto the inner regions (Deason et al. 2013; Pillepich et al. 2015). Inconsistencies in stellar halo definitions can therefore introduce uncertainties into any comparison between observations and simulations or between any two simulations. Of the three simulations that we compare to in Figure 5, Cooper et al. (2010) define the stellar halo as all stellar mass between 3 and 280 kpc; Cooper et al. (2013) measure the stellar mass beyond 3 kpc; and Pillepich et al. (2014) measure the stellar mass beyond 20 kpc. Our method of calculating the stellar mass in excess of a disk+bulge beyond $5R_h$ results in a different physical radius for each galaxy in our sample, with values ranging from 11 to 32 kpc (Table 1).

By design, our calculation of $f_{\rm halo}(> 5R_h)$ does not rely on any assumptions about the global shape of the stellar halo, due to a lack of constraining power in the innermost regions. In the future, a more detailed comparison with simulations might therefore be made by choosing a set of structural parameters, and applying a scaling factor $\kappa = f_{\rm halo}/f_{\rm halo}(> 5R_h)$; doing so would systematically change the halo fractions, but it is unlikely that the RMS scatter would decrease after such a rescaling.

5. CONCLUSIONS

We have presented measurements of the stellar halo mass fraction, defined as the stellar mass in excess of a disk+bulge model outside of $5R_h$, for eight nearby spiral galaxies. Considering the relatively narrow range in stellar mass ($2 - 8 \times 10^{10} M_\odot$), we find a remarkabley wide range in stellar halo mass fractions. One of the galaxies in our sample, NGC 1084, has a stellar halo mass fraction of 0.049 ± 0.02, while three others (NGC 1042, NGC 3351, and M101) have stellar halos that are undetected in our data. We measure an RMS scatter of $1.01^{+0.09}_{-0.26}$ dex, and a peak-to-peak span of a factor of > 100. Placing tighter constraints on the three galaxies that appear to be without stellar halos requires even deeper imaging than what we are presenting here. This will be extremely challenging, but it may be possible with Dragonfly.

The variation in the masses of stellar halos that we find (and implied levels of stochasticity in the accretion histories of these galaxies) is qualitatively consistent with variations in the structure and stellar populations of nearby stellar halos observed in both integrated light and star counts studies (Mouhcine et al. 2007; Tanaka et al. 2011; Barker et al. 2012; Monachesi et al. 2015), although these efforts typically suffer from PSF effects (de Jong 2008; Slater et al. 2009; Sandin 2014; Duc et al. 2015) and sparse area coverage, respectively.

Looking forward, a more comprehensive understanding of the buildup of stellar halos will require not only improved techniques for robust comparisons between observations and simulations, but also a much larger sample of observed stellar halos in order to capture the full extent of the scatter at fixed stellar mass. The advantage of using Dragonfly to study the global properties of stellar halos lies in the combination of its sensitivity, large field of view and relative lack of susceptibility to scattered starlight. Deep integrated light surveys are complementary to resolved star count studies that supply information on the extent and stellar populations of stellar halos in pencil-beam surveys (e.g., GHOSTS; Radburn-Smith et al. 2011). In the future, wide field space-based imaging (with telescopes such as WFIRST) coupled with kinematic data will enable us to characterize the structure and content of a larger sample of stellar halos in the same detail as is possible in the Local Group today.

We thank the anonymous referee for an insightful and thorough report that improved the paper. Support from NSERC, NSF grant AST-1312376 and from the Dun-

lap Institute (funded by the David Dunlap Family) is gratefully acknowledged. All authors thank the staff at New Mexico Skies Observatory for their support and assistance; Andrew Cooper for providing the data necessary to construct the models in Figure 5; and the PAndAS team for providing their M31 star count data. AM thanks the BS group for useful discussions and insights.

APPENDIX

PHOTOMETRIC TESTS

All of the galaxies in our sample are well known, and well studied. We therefore carried out careful comparisons with previously published surface brightness profiles to ensure that our profiles are consistent with existing photometry.

We went about this in two ways − first, we compared directly to profiles found in the literature. As discussed in the main text, M101 has been studied previously by e.g. Mihos et al. (2013) and van Dokkum et al. (2014). Pohlen & Trujillo (2006) published g-band surface brightness profiles of NGC 1042 and NGC 1084; Watkins et al. (2014) derived B-band surface brightness profiles for NGC 3351 and NGC 3368; and a B-band profile of NGC 4258 is presented in Watkins et al. (2016).

Figure 6 shows our surface brightness profiles with these literature profiles superimposed (we applied arbitrary offsets to each profile to avoid confusion between different galaxies). Where existing profiles are measured in B-band, we use the available $B-V$ profiles to convert to g-band, applying conversions from Blanton & Roweis (2007). The agreement between Dragonfly and literature profiles is generally good, with the exception of NGC 3351 and 3368, for which the profiles presented in Watkins et al. (2014) appear to have a systematic offset of 0.5 magnitudes. We note that the apparent disagreement between our results and those of Watkins et al. (2016) for NGC 4258 at large radii is due to differences in averaging; Watkins et al. (2016) measure the median flux in elliptical annuli, whereas we measure the mean.

As a second, independent approach, we also derived surface brightness profiles for the (relatively) high surface brightness regions of the galaxy using SDSS images; these are indicated in Figure 6 as blue lines. We find very good agreement here between the SDSS and Dragonfly profiles. In particular, we note that the surface brightness profiles of NGC 3351 and NGC 3368, which are somewhat in tension with the converted B-band profiles of Watkins et al. (2014), are consistent with the SDSS g-band surface brightness profiles.

REFERENCES

Abadi, M. G., Navarro, J. F., & Steinmetz, M. 2006, MNRAS, 365, 747
Abadi, M. G., Navarro, J. F., Steinmetz, M., & Eke, V. R. 2003, ApJ, 597, 21
Abazajian, K. N., Adelman-McCarthy, J. K., Agüeros, M. A., et al. 2009, ApJS, 182, 543
Abraham, R. G., & van Dokkum, P. G. 2014, PASP, 126, 55
Amorisco, N. C. 2015, ArXiv e-prints
Bailin, J., Bell, E. F., Chappell, S. N., Radburn-Smith, D. J., & de Jong, R. S. 2011, ApJ, 736, 24
Bailin, J., Bell, E. F., Valluri, M., et al. 2014, ApJ, 783, 95
Bakos, J., & Trujillo, I. 2012, ArXiv e-prints
Bakos, J., Trujillo, I., & Pohlen, M. 2008, ApJ, 683, L103
Barker, M. K., Ferguson, A. M. N., Irwin, M., Arimoto, N., & Jablonka, P. 2009, AJ, 138, 1469
Barker, M. K., Ferguson, A. M. N., Irwin, M. J., Arimoto, N., & Jablonka, P. 2012, MNRAS, 419, 1489
Barteldrees, A., & Dettmar, R.-J. 1994, A&AS, 103
Bell, E. F., & de Jong, R. S. 2001, ApJ, 550, 212
Bell, E. F., Zucker, D. B., Belokurov, V., et al. 2008, ApJ, 680, 295
Belokurov, V., & Koposov, S. E. 2016, MNRAS, 456, 602
Belokurov, V., Zucker, D. B., Evans, N. W., et al. 2006, ApJ, 642, L137
Bland-Hawthorn, J., Vlajić, M., Freeman, K. C., & Draine, B. T. 2005, ApJ, 629, 239
Blanton, M. R., & Roweis, S. 2007, AJ, 133, 734
Bovy, J., Rix, H.-W., & Hogg, D. W. 2012, ApJ, 751, 131
Brinchmann, J., Charlot, S., White, S. D. M., et al. 2004, MNRAS, 351, 1151
Brook, C. B., Kawata, D., Gibson, B. K., & Freeman, K. C. 2004, ApJ, 612, 894
Carlberg, R. G., Richer, H. B., McConnachie, A. W., et al. 2011, ApJ, 731, 124
Carollo, D., Beers, T. C., Lee, Y. S., et al. 2007, Nature, 450, 1020
Carollo, D., Beers, T. C., Chiba, M., et al. 2010, ApJ, 712, 692
Chabrier, G. 2003, PASP, 115, 763
Comerón, S., Elmegreen, B. G., Knapen, J. H., et al. 2011, ApJ, 741, 28
Cooper, A. P., D'Souza, R., Kauffmann, G., et al. 2013, MNRAS, 434, 3348
Cooper, A. P., Cole, S., Frenk, C. S., et al. 2010, MNRAS, 406, 744
Courteau, S., Widrow, L. M., McDonald, M., et al. 2011, ApJ, 739, 20
Dalcanton, J. J., & Bernstein, R. A. 2002, AJ, 124, 1328
de Jong, R. S. 2008, MNRAS, 388, 1521
De Lucia, G., & Helmi, A. 2008, MNRAS, 391, 14

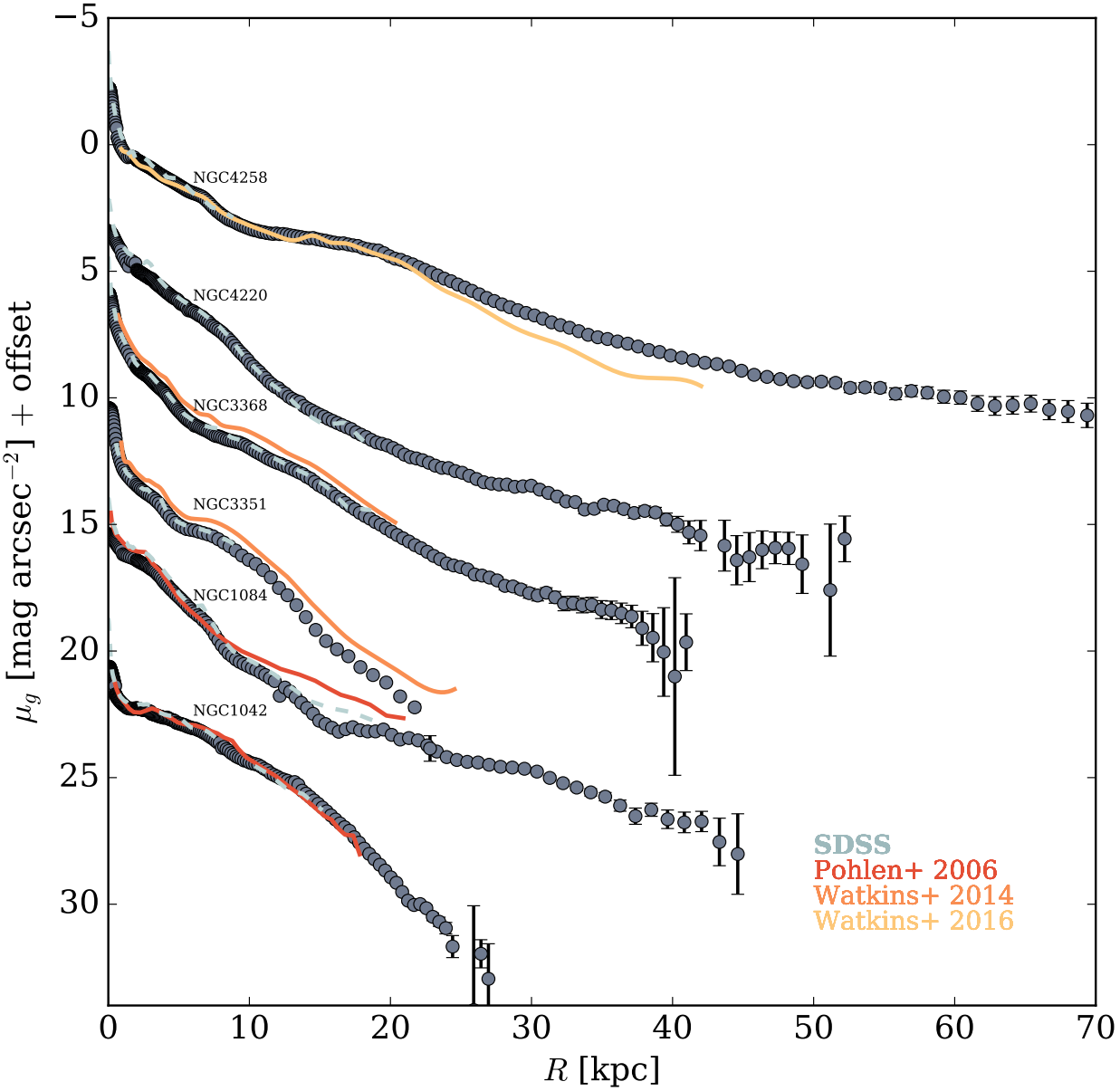

Figure 6. A comparison between Dragonfly g-band surface brightness profiles (grey points) and profiles obtained from the literature. Arbitrary offsets have been applied to each profile to avoid confusion. Additional comparisons to SDSS data are shown as blue dashed lines. We find good agreement with our photometry in both cases.

Deason, A. J., Belokurov, V., Evans, N. W., & Johnston, K. V. 2013, ApJ, 763, 113
Dorman, C. E., Widrow, L. M., Guhathakurta, P., et al. 2013, ApJ, 779, 103
Duc, P.-A., Cuillandre, J.-C., Karabal, E., et al. 2015, MNRAS, 446, 120
Feigelson, E. D., & Nelson, P. I. 1985, ApJ, 293, 192
Ferguson, A. M. N., Irwin, M. J., Ibata, R. A., Lewis, G. F., & Tanvir, N. R. 2002, AJ, 124, 1452
Font, A. S., McCarthy, I. G., Crain, R. A., et al. 2011, MNRAS, 416, 2802
Foreman-Mackey, D., Hogg, D. W., Lang, D., & Goodman, J. 2013, PASP, 125, 306
Gilbert, K. M., Guhathakurta, P., Beaton, R. L., et al. 2012, ApJ, 760, 76
Goodman, J., & Weare, J., 2010, Communications in Applied Mathematics and Computational Science, 5, 65
Greggio, L., Rejkuba, M., Gonzalez, O. A., et al. 2014, A&A, 562, A73
Ibata, R., Irwin, M., Lewis, G., Ferguson, A. M. N., & Tanvir, N. 2001, Nature, 412, 49
Ibata, R., Martin, N. F., Irwin, M., et al. 2007, ApJ, 671, 1591
Irwin, M. J., Ferguson, A. M. N., Ibata, R. A., Lewis, G. F., & Tanvir, N. R. 2005, ApJ, 628, L105

Johnston, K. V., Bullock, J. S., Sharma, S., et al. 2008, ApJ, 689, 936
Lackner, C. N., Cen, R., Ostriker, J. P., & Joung, M. R. 2012, MNRAS, 425, 641
Laine, J., Laurikainen, E., Salo, H., et al. 2014, MNRAS, 441, 1992
Loebman, S. R., Roškar, R., Debattista, V. P., et al. 2011, ApJ, 737, 8
Majewski, S. R., Skrutskie, M. F., Weinberg, M. D., & Ostheimer, J. C. 2003, ApJ, 599, 1082
Makarov, D., & Karachentsev, I. 2011, MNRAS, 412, 2498
Makarov, D., Prugniel, P., Terekhova, N., Courtois, H., & Vauglin, I. 2014, A&A, 570, A13
Martín-Navarro, I., Trujillo, I., Knapen, J. H., Bakos, J., & Fliri, J. 2014, MNRAS, 441, 2809
Martín-Navarro, I., Bakos, J., Trujillo, I., et al. 2012, MNRAS, 427, 1102
Martínez-Delgado, D., Gabany, R. J., Crawford, K., et al. 2010, AJ, 140, 962
McConnachie, A. W., Chapman, S. C., Ibata, R. A., et al. 2006, ApJ, 647, L25
McConnachie, A. W., Irwin, M. J., Ibata, R. A., et al. 2009, Nature, 461, 66
Mihos, J. C., Harding, P., Spengler, C. E., Rudick, C. S., & Feldmeier, J. J. 2013, ApJ, 762, 82
Miskolczi, A., Bomans, D. J., & Dettmar, R.-J. 2011, A&A, 536, A66
Monachesi, A., Bell, E. F., Radburn-Smith, D., et al. 2015, ArXiv e-prints
Monachesi, A., Bell, E. F., Radburn-Smith, D. J., et al. 2013, ApJ, 766, 106
Mouhcine, M., Ibata, R., & Rejkuba, M. 2010, ApJ, 714, L12
Mouhcine, M., Rejkuba, M., & Ibata, R. 2007, MNRAS, 381, 873
Okamoto, S., Arimoto, N., Ferguson, A. M. N., et al. 2015, ApJ, 809, L1
Peñarrubia, J., McConnachie, A., & Babul, A. 2006, ApJ, 650, L33
Pillepich, A., Madau, P., & Mayer, L. 2015, ApJ, 799, 184
Pillepich, A., Vogelsberger, M., Deason, A., et al. 2014, MNRAS, 444, 237
Pohlen, M., Dettmar, R.-J., & Lütticke, R. 2000, A&A, 357, L1
Pohlen, M., & Trujillo, I. 2006, A&A, 454, 759
Purcell, C. W., Bullock, J. S., & Kazantzidis, S. 2010, MNRAS, 404, 1711
Purcell, C. W., Bullock, J. S., & Zentner, A. R. 2007, ApJ, 666, 20
Radburn-Smith, D. J., de Jong, R. S., Seth, A. C., et al. 2011, ApJS, 195, 18
Radburn-Smith, D. J., Roškar, R., Debattista, V. P., et al. 2012, ApJ, 753, 138
Read, J. I., Lake, G., Agertz, O., & Debattista, V. P. 2008, MNRAS, 389, 1041
Richardson, J. C., Ferguson, A. M. N., Johnson, R. A., et al. 2008, AJ, 135, 1998
Ruiz-Lara, T., Pérez, I., Florido, E., et al. 2016, MNRAS, 456, L35
Seth, A., de Jong, R., Dalcanton, J., & GHOSTS Team. 2007, in IAU Symposium, Vol. 241, IAU Symposium, ed. A. Vazdekis & R. Peletier, 523–524
Sandin, C. 2014, A&A, 567, 97
Seth, A. C., Dalcanton, J. J., & de Jong, R. S. 2005, AJ, 130, 1574
Shang, Z., Zheng, Z., Brinks, E., et al. 1998, ApJ, 504, L23
Sheffield, A. A., Majewski, S. R., Johnston, K. V., et al. 2012, ApJ, 761, 161
Slater, C. T., Harding, P., & Mihos, J. C. 2009, PASP, 121, 1267
Streich, D., de Jong, R. S., Bailin, J., et al. 2015, ArXiv e-prints
Tanaka, M., Chiba, M., Komiyama, Y., Guhathakurta, P., & Kalirai, J. S. 2011, ApJ, 738, 150
Tully, R. B., Rizzi, L., Shaya, E. J., et al. 2009, AJ, 138, 323
van der Kruit, P. C. 1979, A&AS, 38, 15
van der Kruit, P. C., & Searle, L. 1982, A&A, 110, 61
van Dokkum, P. G., Abraham, R., & Merritt, A. 2014, ApJ, 782, L24
Vlajić, M., Bland-Hawthorn, J., & Freeman, K. C. 2011, ApJ, 732, 7
Watkins, A. E., Mihos, J. C., & Harding, P. 2016, ArXiv e-prints
Watkins, A. E., Mihos, J. C., Harding, P., & Feldmeier, J. J. 2014, ApJ, 791, 38
Yoachim, P., & Dalcanton, J. J. 2006, AJ, 131, 226
Zheng, Z., Thilker, D. A., Heckman, T. M., et al. 2015, ApJ, 800, 120
Zolotov, A., Willman, B., Brooks, A. M., et al. 2009, ApJ, 702, 1058

Galaxy Name	α	δ	M_B [mag]	D [Mpc]	$N_{\rm member}$	$M_{\rm stell}$ $[M_\odot]$	$5R_h$ [kpc]	$f_{\rm halo}(>5R_h)$
NGC 1042	2 : 40 : 23.97	−8 : 26 : 01.13	−20.27	17.3	6	$1.53 \pm 0.48 \times 10^{10}$	26.6	0.0001 ± 0.0001
NGC 1084	2 : 45 : 59.92	−7 : 34 : 43.10	−20.41	17.3	10	$4.32 \pm 1.41 \times 10^{10}$	17.0	0.049 ± 0.023
NGC 2903	9 : 32 : 10.11	+21 : 30 : 02.99	−20.3	8.5	1	$4.94 \pm 1.57 \times 10^{10}$	19.5	0.0104 ± 0.0072
NGC 3351	10 : 43 : 57.73	+11 : 42 : 13.00	−20.36	10.0	9	$5.84 \pm 1.95 \times 10^{10}$	10.4	0.0002 ± 0.0225
NGC 3368	10 : 46 : 45.74	+11 : 49 : 11.78	−20.03	7.24	9	$8.91 \pm 2.87 \times 10^{10}$	12.8	0.0037 ± 0.0292
NGC 4220	12 : 16 : 11.73	+47 : 53 : 00.07	−19.31	17.1	2	$6.11 \pm 1.96 \times 10^{10}$	13.7	0.0133 ± 0.0109
NGC 4258	12 : 18 : 57.62	+47 : 18 : 13.39	−20.2	7.61	7	$7.61 \pm 2.42 \times 10^{10}$	20.8	0.003 ± 0.0159
M101	14 : 03 : 12.58	+54 : 20 : 55.50	−20.2	7.0	2	$5.89 \pm 1.87 \times 10^{10}$	32.7	0.0004 ± 0.0008

Table 1
Properties of the sample. The stellar halo fractions for M101, NGC 1042 and NGC 3351 are upper limits. Magnitudes and distances were obtained from the Extragalactic Distance Database Tully et al. (2009); group members were obtained from the MK Groups catalog Makarov & Karachentsev (2011).

Galaxy Name	$R_{\rm arm}$ [kpc]	R_2 [kpc]	A_d [$M_\odot$ kpc^{-2}]	R_s [kpc]	A_b [$M_\odot$ kpc^{-2}]	R_e [kpc]	n	A	B
NGC 1042	15.0	24.9	$3.9^{+0.2}_{-0.2} \times 10^8$	$3.0^{+0.1}_{-0.1}$	$1.3^{+0.8}_{-0.3} \times 10^9$	$1.1^{+0.2}_{-0.1}$	$0.9^{+0.4}_{-0.2}$	$-9.5^{+1.9}_{-1.3}$	$17.4^{+1.7}_{-2.6}$
NGC 1084	6.0	43.3	$2.3^{+0.4}_{-0.4} \times 10^9$	$2.0^{+0.2}_{-0.2}$	$3.2^{+1.4}_{-1.3} \times 10^9$	$2.3^{+1.1}_{-0.9}$	$1.3^{+0.5}_{-0.5}$	$-3.3^{+0.2}_{-0.2}$	$10.4^{+0.3}_{-0.3}$
NGC 2903	20.0	40.6	$1.8^{+0.2}_{-0.2} \times 10^9$	$2.9^{+0.1}_{-0.1}$	$1.0^{+0.1}_{-0.1} \times 10^{10}$	$1.5^{+0.4}_{-0.3}$	$0.8^{+0.2}_{-0.2}$	$-6.3^{+0.5}_{-0.5}$	$14.7^{+0.7}_{-0.7}$
NGC 3351	12.0	22.8	$7.5^{+2.9}_{-2.9} \times 10^8$	$2.9^{+0.5}_{-0.3}$	$6.8^{+4.1}_{-2.1} \times 10^{10}$	$1.7^{+0.2}_{-0.2}$	$1.7^{+0.4}_{-0.3}$	$-8.7^{+2.7}_{-1.8}$	$16.6^{+2.4}_{-3.7}$
NGC 3368	12.0	37.1	$4.5^{+3.5}_{-1.8} \times 10^8$	$4.3^{+1.0}_{-0.8}$	$8.1^{+0.9}_{-1.4} \times 10^{10}$	$2.7^{+0.2}_{-0.2}$	$1.9^{+0.1}_{-0.2}$	$-4.6^{+1.0}_{-1.0}$	$12.3^{+1.6}_{-1.5}$
NGC 4220	4.5	41.2	$3.3^{+0.5}_{-1.1} \times 10^9$	$2.3^{+0.3}_{-0.1}$	$5.1^{+1.3}_{-1.2} \times 10^9$	$2.6^{+2.3}_{-1.0}$	$0.9^{+0.4}_{-0.3}$	$-4.0^{+0.2}_{-0.2}$	$11.3^{+0.2}_{-0.2}$
NGC 4258	28.0	69.4	$6.0^{+0.5}_{-0.5} \times 10^8$	$5.3^{+0.1}_{-0.1}$	$2.5^{+0.0}_{-0.1} \times 10^{10}$	$3.9^{+0.0}_{-0.1}$	$1.7^{+0.1}_{-0.1}$	$-3.9^{+0.4}_{-0.4}$	$11.8^{+0.6}_{-0.6}$
M101	40.0	41.9	$5.2^{+0.3}_{-0.4} \times 10^8$	$4.1^{+0.1}_{-0.1}$	$9.0^{+4.9}_{-2.8} \times 10^9$	$1.5^{+0.3}_{-0.3}$	$1.9^{+0.5}_{-0.4}$	$-9.5^{+0.5}_{-0.2}$	$19.5^{+0.4}_{-0.8}$

Table 2
Parameters from the best fit disk+bulge model and power law extrapolation. The projected radii at which the last visible spiral arms are located and the signal to noise ratio drops below 2 are given by $R_{\rm arm}$ and R_2, respectively.